Flow Measurements on a Turbulent Fiber Suspension by Laser Doppler Anemometry

Sven R. Andersson and Anders Rasmuson
Dept. of Chemical Engineering Design, Chalmers University of Technology, S-412 96 Göteborg, Sweden

The flow and transition of fiber suspensions to turbulence in a rotary shear tester were studied. Both torque and LDA measurements were performed on a refractive-index-matched glass-fiber suspension in the 3–20 wt. % concentration range. The flow of such suspensions underwent two transitions: the first one coincided with complete agitation, a sharp increase in torque, and fluctuating velocities close to zero. The mean velocities were similar to those of single-phase flow above this transition. The fluctuation velocities approached those of single-phase flow with increasing rotational speed, until they were nearly equal. This second transition was interpreted as fully developed turbulent flow. CFD, assuming single-phase flow, is a helpful tool for describing the flow behavior in this region. The network strength was useful for the study of flow transitions. LDA measurements of the boundary layer at the bottom wall showed that the velocity profile is linear close to the wall even with fibers present. The presence of the fibers also flattened the profiles, indicating an increased momentum transfer.

Introduction

Fiber suspensions are of importance in many fields of chemical engineering, for example, pulp, paper, food, polymer, and biotechnical applications. This study is somewhat focused on pulp and paper applications, although most of the results are of general importance.

Wahren (1980) suggested that unit operations handling pulp-fiber suspensions could be considerably more efficient if the fiber concentration was increased. Gullichsen and Härkönen presented pioneering work in 1981, in which they showed that the flow of a medium consistency (MC; that is, in the concentration range 10–20 wt. %) fiber suspension, resembles that of water at high enough shear rates. This was a starting point for the introduction of MC technology, which has led to a decrease in apparatus dimensions and water consumption. The water-resembling behavior was later called ''fluidization,'' a term criticized by Duffy (1993) for being imprecise, since several definitions have been used. Fluidization was initially attributed to a sharp change in torque, which coincided with fully turbulent flow throughout the vessel and complete fiber dispersion (that is, the individual fibers are moving relative to each other). Bennington et al. (1991) continued studying the flow of pulp suspensions in rotary devices with different gap sizes between the rotor and the outer walls. They found that the change in torque could be attributed to a change in the flow pattern from tangential to outward radial flow. They also found discrete flocs at the fluidization point. Bennington and Kerekes (1996) compared different criteria for the energy dissipation required for fluidization with experimental results. The fundamental mechanisms are, however, still poorly understood. Steen (1989b) concluded that there is no thorough discussion on turbulent fiber suspensions in the literature, which is not surprising considering the complexity of the subject. Two-phase flows in general have attracted a lot of attention from researchers in the past decades. Turbulence in dense suspensions is encountered in gas–solid fluidization [such as Enwald et al. (1996) for a review of the field].

Detailed flow measurements, such as velocity profiles and turbulence, have been reported only during the past two decades. Ek et al. (1978) measured the dilute suspensions of fibers in air with laser Doppler anemometry (LDA). Kerekes and Garner (1982) used LDA in a 0.5% pulp-fiber suspension. The concentration and penetration depth of LDA measurements are severely limited by the light-scattering properties of pulp fibers. A remedy is to use a model suspension, which was done by Steen (1989a). He used glass fibers in a mixture of ethanol and benzyl alcohol, which then had the

Correspondence concerning this article should be addressed to A. Rasmuson.

same refractive index as the fibers. Steen (1989b) used LDA in order to measure mean velocities, fluctuating velocities, and turbulence spectra of 1.2 and 12 g/L glass-fiber suspensions flowing in a pipe. He found higher turbulent energy at low concentrations and short fibers, compared to higher concentrations and/or longer fibers.

Li et al. (1994) used the nuclear magnetic resonance (NMR) technique to obtain mean velocity profiles of pulp-fiber suspensions in pipe flow at less than 1 wt. %. McComb (1991) discusses turbulence modification in drag-reducing asbestos fiber suspensions at fiber concentrations of 0.03 wt. %, for which turbulence spectra have been measured by LDA. He concludes that there is an increase in turbulence intensity at low and high wave numbers, but that turbulence is suppressed by resonant absorption of turbulent energy by the fibers in a region comparable to the fiber length.

None of these earlier studies has related the transition to turbulence to local flow properties. The objective of this work was to measure flow properties of the continuous phase with the LDA technique, and to compare the results with CFD calculations. This was done by combining the index-matching technique developed by Steen (1989a) with the geometries studied by Gullichsen and Härkönen (1981) and Bennington et al. (1991). The ultimate goal is to obtain better criteria for the transition to fully developed turbulent flow and, thus, a framework for better apparatus design.

Theory

In a single-phase Newtonian fluid, the transition to turbulence is governed by the ratio of inertial to viscous forces, that is, the Reynolds number. A fiber suspension normally has a Newtonian continuous phase, but the fiber network imposes further resistance to movement.

Fiber networks

The network strength (yield stress) is defined as the shear force required to disrupt the fiber network and is, according to present view (Bennington et al., 1990), caused by the mechanical entanglement of fibers. Fibers are locked into their positions by the constraints imposed by neighboring fibers. These constraints cause the fibers to become deformed, resulting in normal forces in the fiber–fiber contact points. The frictional force in these contact points imposes resistance to movement and results in network strength. In a previous work, the friction of pulp fibers was measured (Andersson and Rasmuson, 1997; Andersson et al., 2000), and a network strength model is presented by Andersson et al. (1999). The average distance between the contact points of a fiber is called the segment length.

Transition to turbulence

The fiber network imposes resistance to turbulent flow on several different length scales. On the largest scale, the shear force must be larger than the network strength in order to achieve motion. On scales smaller than the fiber length scale, the single fibers cannot follow the flow entirely, which gives rise to relative velocities. This draws power from the fluctuations at that scale.

As indicated in the Introduction, the definition of the transition to turbulence is a subject of some controversy. Wahren (1980) presented a map of energy dissipation vs. concentrations in various equipment used in the pulp and paper industry. He used the onset of drag reduction in pipe flow to calculate an expression for the total energy dissipation, ϵ_F [W/m^3] at which fiber dispersion occurs:

$$\epsilon_F = \frac{\tau_y^2}{\mu} \approx 11.6\times 10^3 \cdot C_m^{5.28}, \tag{1}$$

where C_m is the mass concentration of the suspension in percent. The first part of Eq. 1 is discussed and criticized extensively in the water flocculation literature (such as Clark, 1985). The second equality follows from empirical correlations for the yield stress and the viscosity of water. Wahren's choice of using the viscosity of water is criticized by Bennington and Kerekes (1996). They use the power dissipation rate per unit volume to characterize the turbulence in a concentric cylinder system. Using this approach, the power dissipation rate per unit volume [W/m^3] was found empirically to be

$$\begin{gathered}\epsilon_F = 4.5\times 10^4 C^{2.5} \left(D_T/D\right)^{-2.3} \\ 1.3 \le D_T/D \le 3.1; \quad 1.0 \le C[\%] \le 12.6,\end{gathered} \tag{2}$$

where D_T/D is the rotor to vessel ratio. Further, they compared Wahren's expression with one they obtained from the work by Gullichsen and Härkönen (1981):

$$\epsilon_F = 3.4\times 10^2 C_m^{3.4}. \tag{3}$$

The reader is referred to Tennekes and Lumley (1992) for an often cited overview of the basics of single-phase turbulence. According to Kolmogorov's well-known theory, turbulent energy is added to eddies of the largest scales present. The energy is then transferred to the eddies of the next smaller size and so on, until the energy is dissipated into heat at the smallest scales of turbulence (the Kolmogorov scale). The dominating mechanism for energy transfer is vortex stretching. This concept is called the energy cascade, and an important consequence is that all of the added energy is dissipated at the smallest scales. The situation is complicated substantially by the presence of fibers.

Two hypotheses as to the mechanism causing the transition to turbulence in fiber suspensions can be envisaged:

1. The transition is governed by the fiber network strength imposing resistance to the largest eddies. In the laminar situation, the network strength governs the transition between flow and stagnation. Eddies with sufficient energy to overcome the network strength will persist much longer, while low-energy eddies will lose all their energy rapidly due to fiber–fiber interactions. A level of turbulent kinetic energy is thereby expected, where more energy is transferred to smaller scales than is lost to fiber–fiber friction. Below this level, turbulence is strongly dampened. We will focus on the largest eddies, since these will have the greatest impact on the macroscopic behavior of the suspension. According to Tennekes and Lumley (1992), the energy transfer from an eddy with a characteristic velocity u and a characteristic length ℓ will be of the order u^3/ℓ (W/kg). Unlike a single-phase flow, the eddies will also lose energy to friction in the interfiber contact points. This manifests itself by an extra dissipation on

this scale. The size of this dissipation may be estimated under the following assumptions: the eddy studied consists of a cylinder of diameter ℓ, length L, and a tangential velocity u. The fiber network inside the eddy moves with the eddy, and all network breakage occurs at the cylindrical surface. The dissipation thus becomes the power lost by the eddy divided by the weight of the eddy:

$$\epsilon_{ys} = \frac{\tau_y \cdot u \cdot \text{Area}}{\text{Weight}} = \frac{\tau_y \cdot u \cdot \pi \cdot \ell \cdot L}{\rho \cdot \pi \cdot L \cdot (\ell/2)^2} = \frac{4 \cdot \tau_y \cdot u}{\rho \cdot \ell}. \quad (4)$$

It is reasonable to assume that the turbulence is strongly suppressed if $\epsilon_{ys} \approx u^3/\ell$, since the eddies then will lose the same amount of energy to the network as to the smaller eddies.

2. The transition is governed by the fiber–fluid drag on the length scale of the fiber segment, ℓ_s, that is, the distance between two consecutive contact points. A relative fiber–fluid velocity perpendicular to the fiber axis exerts a force on the fiber. This force may increase, decrease, or even remove the normal force in the contact point, allowing the fibers to move more freely. This process could be continuous in its nature, increasing the level of fiber disengagement with turbulence fluctuations. A force balance over one fiber segment, that is, the distance between two consecutive contact points, assuming that the fiber is perpendicular to the flow gives:

$$2F_o = d \cdot \ell_s \cdot \rho \cdot C_D \frac{u^2}{2}, \quad (5)$$

where F_o is the minimum force required for the fibers to start sliding (Andersson et al., 1999). The righthand side describes the fiber drag, where $d \cdot \ell_s$ is the projected area of one fiber segment. These hypotheses are tested against experiments.

Boundary layer

Turbulent boundary layers over plates and in pipes are treated in numerous textbooks, notably *Boundary-Layer Theory* by Schlichting (1966). Literature is, however, scarce on boundary-layer flows for more complicated geometries.

The velocity and distance can be nondimensionalized with the friction velocity, u^*, in the near wall region. The linear velocity profile $u^+ = y^+$ is obtained closest to the wall, while the ''law of the wall'' holds further away from the wall:

$$\frac{u}{u^*} = \frac{1}{\kappa_{\text{Kármán}}} \ln y^+ + A, \quad (6)$$

which describes the boundary layers in pipe flow and over flat plates (Schlichting, 1966). A is a constant that depends on wall roughness.

Experimental

Apparatus

A rotating cylinder system similar to the ones used by Gullichsen and Bennington was chosen: the walls and rotor were baffled to prevent wall slip. The optical difficulties involved with using the LDA technique through curved surfaces was avoided by providing the vessel with six flat walls, one consisting of a glass window. The remaining five walls were cooled by tap water in order to maintain a constant temperature throughout the experiments, which is a prerequisite for index matching. Measurements, as a result of symmetry, were only necessary on one-twelfth of the volume. The geometry is shown in Figures 1 and 2. The height of the vessel is 90 mm and that of the rotor is 80 mm, leaving a 5 mm gap below and

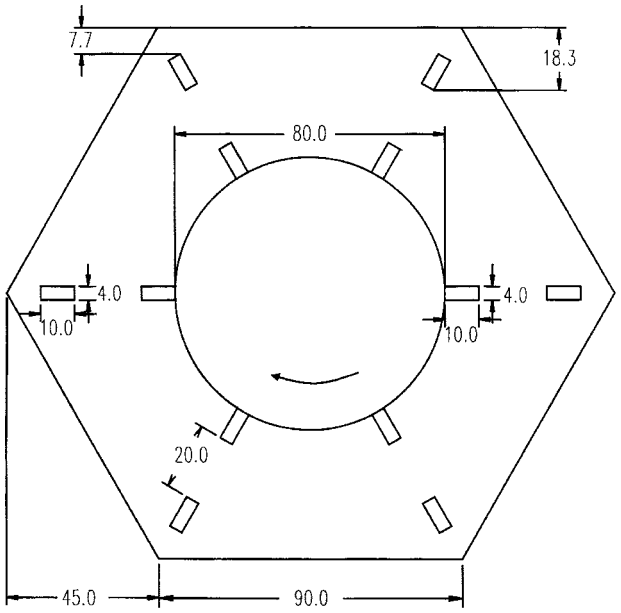

Figure 1. Top view of the geometry of the shear tester.
The measures are in mm. All sharp edges were rounded with a 1-mm radius of curvature.

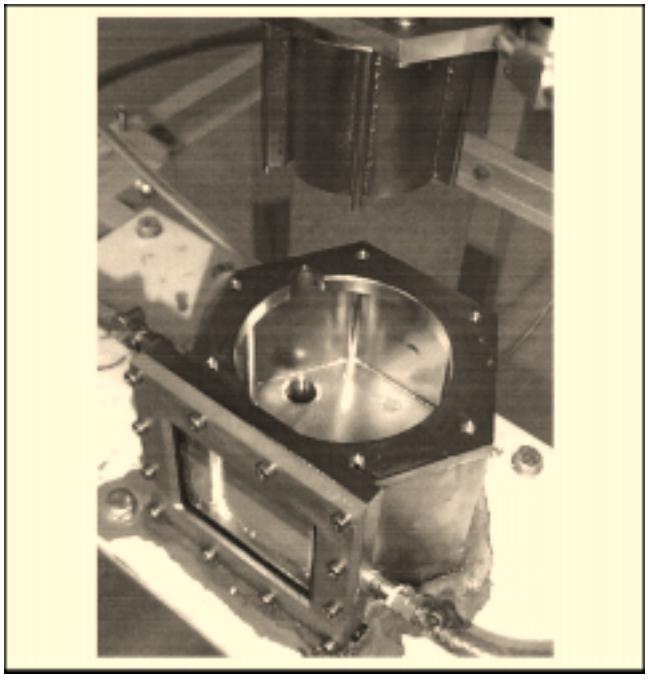

Figure 2. Shear tester.

above the rotor. Some definitions will be made regarding the measurement positions: a plane midway between the top and bottom walls at right angles to the rotor axis is understood to be ''the radial symmetry plane.'' Whenever a radial velocity profile is presented, it has been taken at right angles to the observation glass, at a height between the bottom wall and the radial symmetry plane. The radial position is given as a dimensionless coordinate, where zero represents the observation glass and one represents the rotor tip. A dimensionless radial position of 0.12 has been used for the transition measurements. Tangential velocity (denoted u) is used for a velocity parallel to the observation glass, although it is tangential in a strict sense at only some positions. The rotor moves clockwise, and the tangential direction is defined as positive in this direction. The positive direction of axial velocities is downwards. The vector plots, however, reflect the directions shown by the arrows.

The rotor was driven by a 4-kW electrical motor (ABB, model M2AA 112 M-2) powered by an adjustable frequency shifter (Hitachi, model J100). The motor was supported by bearings, as was the motor axis. The torque was measured by means of a load cell (BLH Electronics, Alfa Load Beam) in contact with a cantilever fastened on the motor. The bearing friction was judged to be low enough to ensure accurate measurements of the torque. The power demand, P, was calculated from the torque (Nm) and the angular velocity (rad/s).

Model suspension

Glass fibers in a refractive-index matched fluid were used as a model system. Efforts were made to achieve an index matched fiber suspension with polymer fibers, as their mechanical properties are closer to those of pulp fibers than glass fibers are. The tested polymer fibers turned out to be highly optically anisotropic due to strongly oriented polymer molecules, a result of severe stretching during the manufacturing procedure. Even the anisotropy of unstretched polymer fibers was large enough to prevent successful index matching. Instead, glass fibers were used. Owens Corning (Huntingdon, PA) provided chopped ''S-2'' fibers, marketed as high tensile strength and fatigue-resistant glass fibers. The diameter of the fibers was 9 μm and lengths of 1.5 mm and 3 mm were used. Owens Corning (1994) report a tensile strength of $4.6-4.8\times10^9$ Pa, an elastic modulus of $8.6-9.0\times10^{10}$ Pa, a density of 2,475 kg/m^3, and a refractive index of 1.523–1.525. The fibers were initially coated with an epoxy resin, which was removed by heating the fibers to 850°C for half an hour. The liquid used was a mixture of benzyl alcohol (BA) and ethanol, with a viscosity of 6.9×10^{-3} Pas and a density of 1022 kg/m^3. The refractive index of the liquid was matched to that of the fibers by changing the composition. Except for a 5 wt. %, 3 mm suspension, 1.5-mm fibers were used everywhere. The 3-mm fibers were plotted at 6 wt. %, since their network strength was 30–40% larger than the corresponding 1.5-mm suspension, which roughly corresponds to a 6 wt. %, 1.5-mm suspension.

Filling

The fibers were chopped from strands of multiple fibers, resulting in dense bundles of strongly oriented fibers. Large numbers of fibers could thus be packed easily into the apparatus without additional force. Once the liquid had been added and the suspension deaerated as described below, the fibers were dispersed by a few seconds' agitation at a high rotational speed.

The air content of a fiber suspension has been shown by Bennington et al. (1995) to influence the hydrodynamic properties greatly. Therefore, the following measures were taken in order to create and maintain a suspension with a low air content. The dry glass fibers were first packed into the apparatus, followed by a very slow pouring of the premixed liquid into the apparatus through a 15-mm opening. Thus, the liquid–air interface moved upwards through the fiber bed, leaving only a few small bubbles in the wetted fiber bed. When the vessel was nearly full, the opening was closed with a screw lid provided with tubes for ethanol, BA, and deaeration, respectively. The main lid of the vessel was roughly conical shaped and provided yet another deaeration channel. The rotor was run a few revolutions at a very low speed, after which most of the bubbles remaining in the fiber network floated up to the conical lid, and could be evacuated.

In situ index matching

The quality of the Doppler signal is strongly dependent on the refractive index matching, which in turn is temperature sensitive. The index matching was judged visually by the dispersion of laser light. A composition of 11.6 wt. % ethanol in benzyl alcohol was found to be optimal. *In situ* index matching was then applied by adding either ethanol or benzyl alcohol while withdrawing fiber-free mixture from a valve covered with a fine mesh. The rotor was run at a low velocity before the network had been dispersed, which allowed the data rate (that is, the number of velocity measurements per second) to be used for the index matching. In contrast to Steen (1989a), the data rate increased with better index matching.

Laser Doppler Anemometry

In LDA, the local velocities in the intersection of two laser beams are determined by analyzing the scattered light from this well-defined measurement volume. The interference pattern of the intersecting laser beams is called fringes. The scattered light from a spherical particle crossing the intersection of the beams will be modulated with the light from the fringes. The modulation frequency is proportional to the speed of the particle.

The laser Doppler anemometer used in this work was a DANTEC FiberFlow Series 60X (Skovlunde, Denmark), which allowed the axial and tangential velocity components to be measured simultaneously. The laser was made by Spectra-Physics (Model 2060A-64, Darmstadt, Germany) and two burst spectrum analyzers (BSA) of the DANTEC 57N10 and 57N25 type were used to extract velocity data from the Doppler signal. A PC was used to store the collected data and to compute moments and spectra. The software used was DANTEC's Burst Ware, Version 3.1. For each measurement, 10,000 velocities were recorded. The velocities were weighted, using the transit time through the measurement volume, in order to correct for the bias originating from the velocity–data-rate correlation.

Table 1. Size of the LDA Measurement Volume

	Tangential Velocity Component	Axial Velocity Component
Tangential size	58 μm	61 μm
Axial size	57 μm	60 μm
Radial size	525 μm	562 μm

A DANTEC lightweight traversing system was used to position the fiberoptic probe. According to the specifications, the resolution was 12.5 μm and the repeatability was 40 μm. The measuring volume size in vacuum is given in Table 1. An angular decoder provided the rotor position in order to resolve periodic fluctuations by providing the data-collection system with 3,600 pulses per revolution.

The suspension was seeded with 2.00 μm spherical silica particles (refractive index = 1.37; Bangs Laboratories Inc., Fishers, IN). Since both the seed particles and the fibers consist mainly of SiO_2, they are likely to have the same surface charge, which means that they are repellents. In other words, the seed particles follow the fluid and not the fibers.

Gravity did not influence the spatial distribution of fibers, since the sedimentation velocity of the suspensions was typically 1 mm/min or slower, which is approximately 10^5 times slower than typical liquid velocities during the experiments. At 5 wt. % and larger, no sedimentation occurred at all.

Data validation

Although a great deal of effort was made to minimize light scattering due to imperfect index matching, the possibility of detecting bursts from fibers raised the question of data reliability. The particle size influences the envelope-to-pedestal ratio (also called visibility) (such as Steen, 1989a). The LDA system allowed the rejection of too large particles by the visibility through setting an "oversize rejection level." The following test was performed in the mixer to ensure that no bursts originated from fibers: the data rate for pure water was recorded as a function of the oversize rejection level and compared with that of 1 wt. % glass fibers in water. The refractive index of the glass fibers differed substantially from that of water (1.52 compared to 1.33), resulting in strong light scattering. The main appearance of the data rate remained the same for the fiber suspension, although the absolute values were lower.

Numerical

The flow field was calculated with the commercial CFD-code, CFX 4.2C, using an HP-735 workstation with 128 MB of RAM. CFX uses the control volume method to discretize the governing equations. The hybrid differencing scheme was applied for all of the variables except pressure, for which central differencing was used. The SIMPLE algorithm was employed to update the pressure and velocity fields in each iteration. The turbulence models used were the standard k-ϵ model, with logarithmic wall functions, and the standard differential Reynolds stress model. The sliding-grid technique was employed, which means that the computational domain is divided into a stationary part (the outer part of the vessel) and a rotating part (following the impeller). The variables are

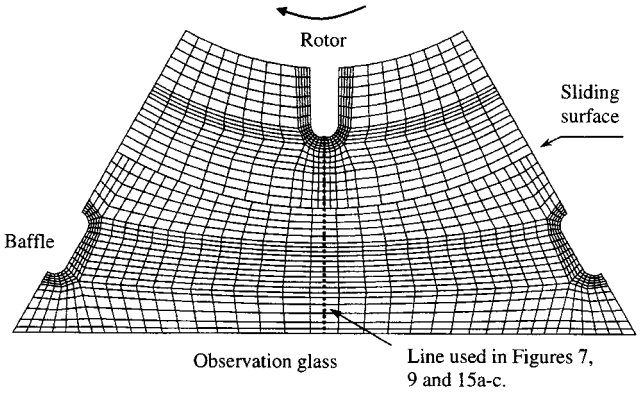

Figure 3. Top view of the computational grid.

interpolated at the sliding surface. Two advantages of using the sliding-grid technique are (1) only wall boundary conditions have to be used, as opposed to measured impeller boundary conditions, and (2) the periodic fluctuations of the flow are resolved. The computational grid consisted of almost 50,000 nodes, the top and side views of which are shown in Figures 3 and 4. As with the measurements, only one-twelfth of the volume had to be treated due to symmetry.

The cylindrical volume below the rotor body was not included in the calculations. The cylindrical rotor was extended all the way down to the bottom wall instead; a free-slip boundary condition was employed at the area thus introduced. One hundred and twenty time steps per revolution were used, which roughly corresponds to the rotating grid revolving one node. One revolution required approximately 12 h of CPU time.

The calculations were carried out until the periodic variations of all the variables in the monitor points were stable. The convergence criterion used for each time step was a mass-residual sum of less than 0.01% of the total mass. A monitoring point was chosen at the sliding-grid interface, in

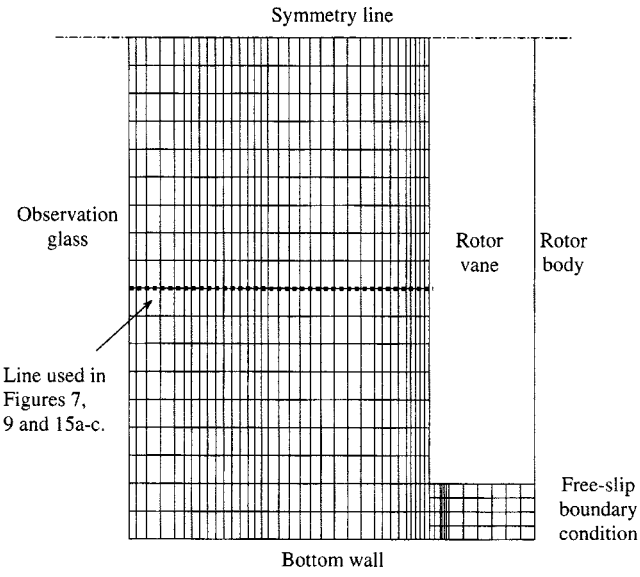

Figure 4. Side view of the computational grid.

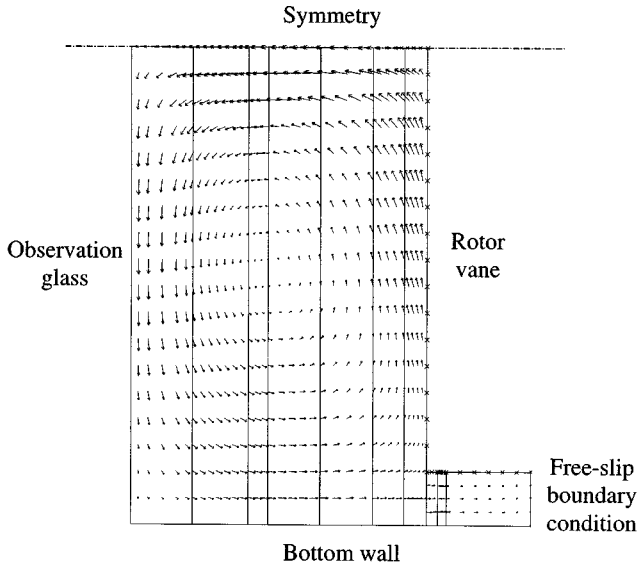

Figure 5. Side view of the calculated velocity field.

It demonstrates the outward radial flow at the radial symmetry plane and the recirculation at the bottom.

the radial symmetry plane. All values at this position had converged to the four figures displayed within ten iterations, except for the tangential velocity and the pressure, which required 20 iterations. Between 40 and 150 iterations were made for each time step, except at startup, where more iterations were required.

Results

The impeller produces a strong tangential velocity component and an outward radial flow, which is shown in Figure 5. The tangential flow can be seen in Figure 6.

Single-phase measurements vs. calculations

The overall trend from the comparisons between single-phase measurements and CFD calculations is that the values from the calculations are approximately 25% too low, whereas the general appearance agrees well. The mean velocities predicted by the differential Reynolds stress model deviated slightly more from the measurements than did the k-ϵ model, while the root mean square (rms) values were far too low. In Figure 7, calculated (k-ϵ) and measured mean and rms velocities are shown at a radial line perpendicular to the observation glass and 25% from the bottom. The calculated mean value of the energy dissipation was 56 W/kg, while the measured value was 89 W/kg at 17 rps.

The influence of the periodic fluctuations on the mean and apparent turbulent fluctuating velocities was studied by means of the angular decoder described earlier. Since most of the apparatus volume can be considered to be close to the rotor, the periodically fluctuating component was expected to be large. The dimensionless tangential velocity is shown as a function of rotor angle and radial position in Figure 8, where both measured and calculated values are shown. The axial and tangential positions are at a height of 25% from the bottom wall and perpendicular to the observation glass. A rotor

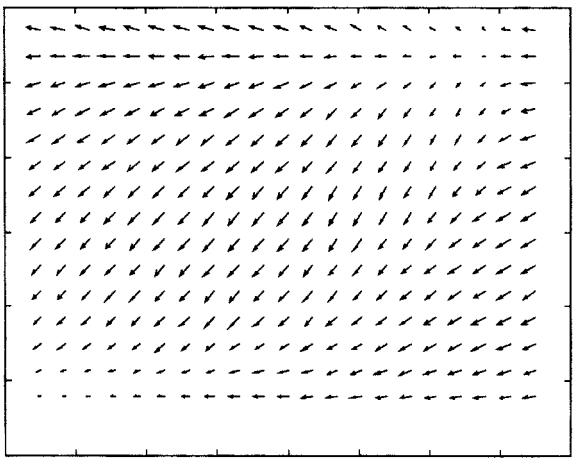

Figure 6. Measured (LDA) single-phase velocity field parallel to the observation glass.

The plot shows the lower half of the observation glass at 25 rps and the dimensionless radial position 0.12.

angle of zero corresponds to the rotor vane being between the baffles. The main appearance is predicted by the calculations, but the absolute values are too low. Close to the rotor, the velocity increases just after the vane has swept by. Measured and calculated mean and fluctuating tangential velocities are shown in Figure 9, for both one rotor position and the mean values for one revolution. At a rotor angle of zero, both the measured and calculated mean velocities were lower than the averaged ones close to the rotor, but nearly identical at the outer half. Weighting the averaged values yielded a constant decrease by 10%. The rms values were practically unaffected by weighting and averaging. The reason for choosing the tangential velocity is that tangential momentum is added by the impeller in a periodic way. A comparison showed that the axial periodic component was actually smaller.

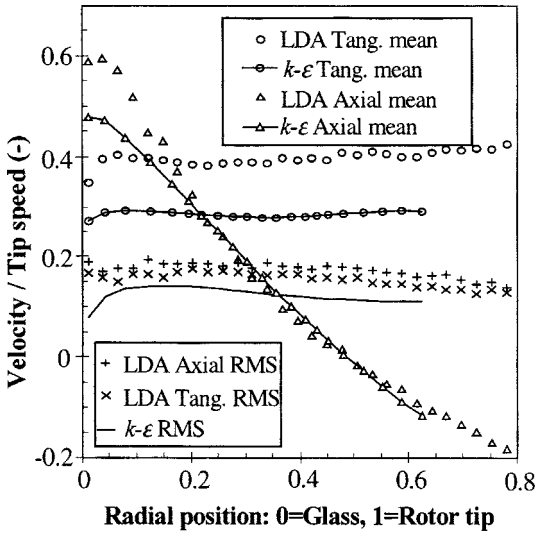

Figure 7. Single-phase LDA measurements vs. k-ϵ calculations at the line in Figures 3 and 4.

The values are averaged over all impeller positions.

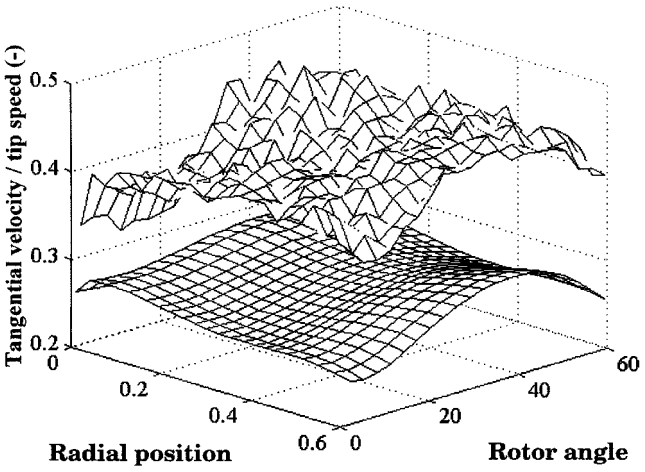

Figure 8. Tangential velocity as a function of rotor angle (degrees) and radial position in Figures 3 and 4 (1 = rotor wall and 0 = glass).

The upper values are unweighted experimental data for single-phase flow, while the lower ones are calculated with the k-ϵ model.

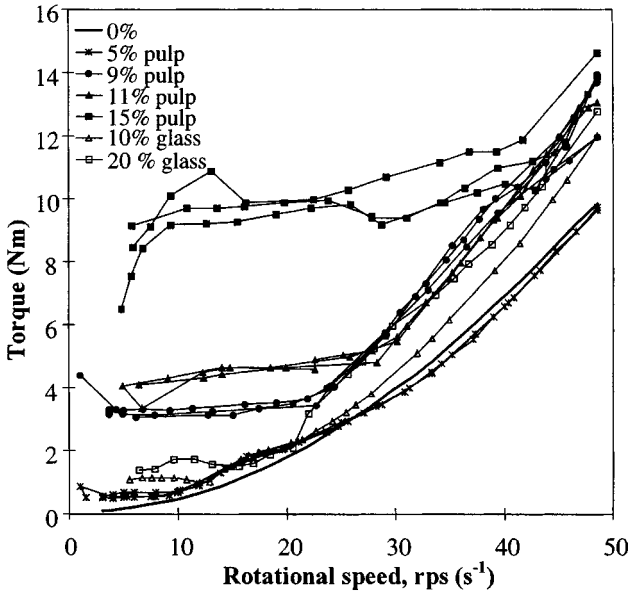

Figure 10. Torque as a function of the rotational speed of single-phase compared to softwood kraft pulp and 1.5-mm glass-fiber suspensions.

The concentrations are given as wt. %.

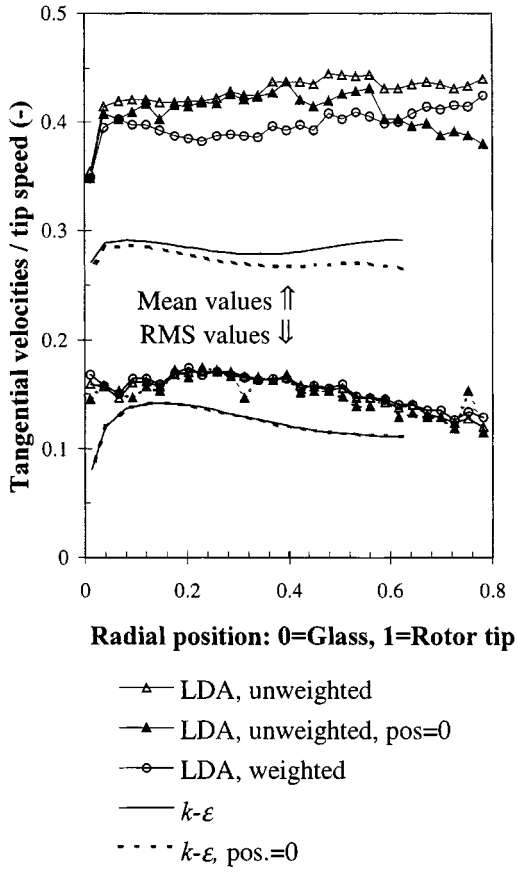

Figure 9. Measured vs. calculated mean and fluctuating tangential velocities for single-phase flow at the line in Figures 3 and 4.

Further, the values at one rotor position are compared to those averaged over one revolution.

Flow regimes in fiber suspensions

In fully developed, turbulent, single-phase flow, both mean velocities and rms velocities are proportional to the tip speed. In a fiber suspension, however, the turbulence is expected to be strongly influenced by the presence of fibers. The torque is shown in Figure 10 as a function of the rotational speed for a number of suspensions. The torque is approximately constant in a range of rotational speeds up to the "fluidization" point, above which the torque increases. In agreement with Bennington et al.'s (1991), but in contrast to Gullichsen and Härkönen's (1981), results, the torque is significantly larger than for that of single-phase flow. The discrepancies between glass- and pulp-fiber suspensions at similar concentrations are analyzed in the discussion section.

The measured rms values of a 10 wt. % glass-fiber suspension, together with single-phase flow, are presented in Figure 11 as a function of the rotational speed. At low rotational speeds, the fluctuations are dampened in the fiber suspension. A purely empirical equation consisting of two straight lines (one of which intersects the origin) was fitted to each rms-velocity component. The intersection of the lines (u': 37.3 rps; v': 33.5 rps) was interpreted as the transition to fully turbulent flow, above which it resembles 0%. The intersection of the lower-end line with the abscissa (for $u' = 0$ and $v' = 0$, the rotational speed was 13.0 rps) was initially interpreted as laminar flow, until it was discovered that the point coincided with a sudden increase in torque, which was defined as the fluidization point by Gullichsen!

The energy dissipation at the transition points of pulp- and glass-fiber suspensions are plotted in Figure 12 and compared with the values given by Eqs. 1–3, the last of which compares well. It is seen that the two transition points show similar trends vs. concentration. The transition points of the pulp-fiber suspensions were defined by the sudden increase

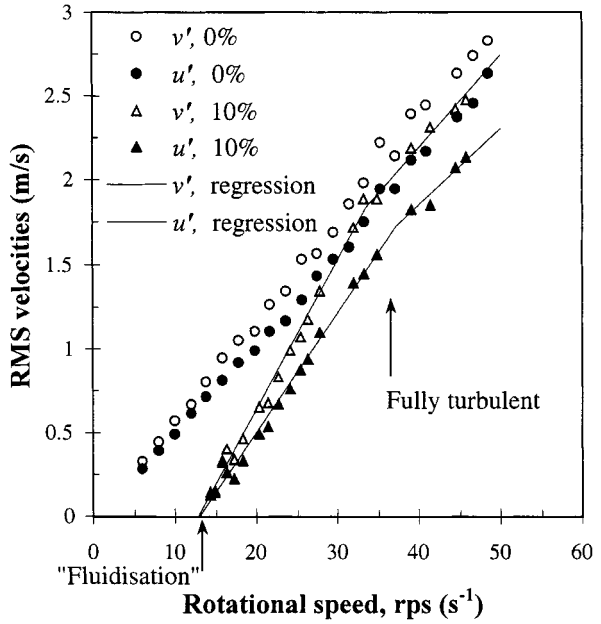

Figure 11. Rms velocities for single-phase together with a 10 wt. % glass-fiber suspension as a function of rotor speed.

Measured at a dimensionless radial position of 0.12. v' is axial and u' is tangential rms velocity.

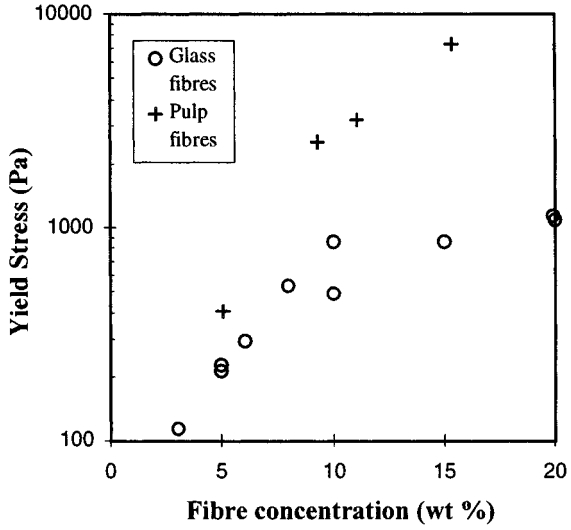

Figure 13. Yield stress of glass and pulp-fiber suspensions, evaluated from torque measurements.

in torque, following Gullichsen and Härkönen (1981). The pulp suspension fluidization transitions from Figure 10 were found to lie between the two glass-fiber transitions at the same mass concentration. Comparing the yield stress of the pulp- and glass-fiber suspensions given in Figure 13, however, gives a lower value for the glass fibers at the same mass concentration. This means that a pulp suspension should be compared to a glass-fiber suspension of larger concentration. In that case, the pulp suspension transitions become more comparable to the glass-fiber "fluidization" transitions. In Figure 14, the transitions have been plotted against the yield stress. Gullichsen and Härkönen's (1981) values compare very well with our pulp-fiber measurements, while Bennington et al.'s (1991) values are higher. The glass-fiber fluidization points for 5–10 wt. % follow the trend of our and Gullichsens pulp measurements, while the values for 15 wt % are closer to Bennington's values. The line $\epsilon = 10^{-4} \cdot \tau_y^2$ correlates to the fluidization points. The dissipation at fully turbulent flow is more than one order of magnitude larger than at fluidization.

The radial flow profiles of a 15 wt. % glass-fiber suspension are presented at 25, 33 and 42 rps in Figures 15a–15c at the line shown in Figures 3 and 4. "Fluidization" occurred at 19.8 rps for u' and at 18.3 rps for v'. The transition to fully

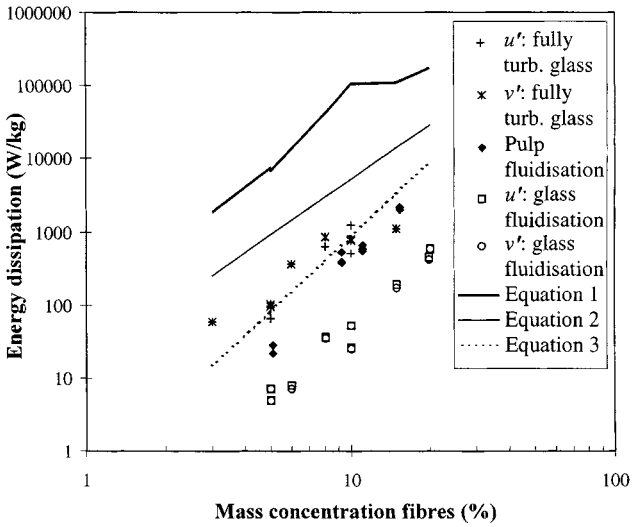

Figure 12. Energy dissipation at fluidization" and fully turbulent flow plotted against the mass concentration of the suspension.

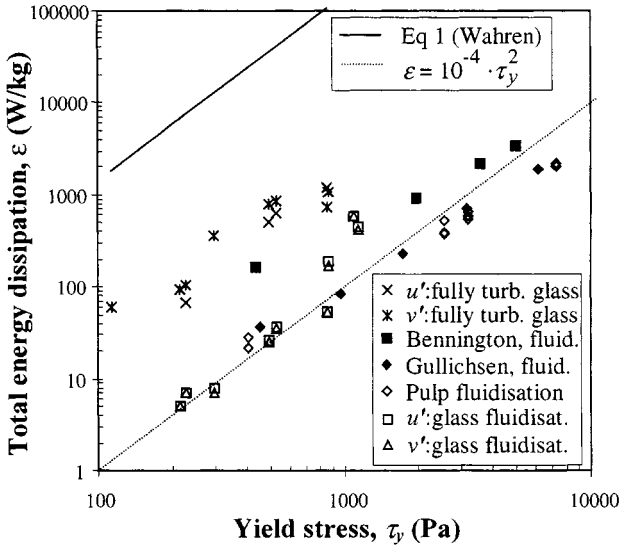

Figure 14. Total energy dissipation for pulp- and glass-fiber suspensions as a function of the yield stress.

turbulent flow occurred at 37.7 rps for u' and at 35.6 rps for v'. The figures consequently represent: (a) just above fluidization; (b) just below the transition to fully turbulent flow; and (c) above the transition to fully turbulent flow. The mean velocities compare well, while the rms velocities of the fiber suspensions are dampened at lower rotational speeds.

Preliminary measurements showed that the largest influence from the fibers could be found just behind the baffles. This area was therefore investigated for the 10 wt. % glass-fiber suspension at a number of rotational speeds. Vector plots of the velocities scaled with tip speed are shown in Figure 16. The flow field can be seen to remain unchanged by the fibers except for 14 rps, where all velocities are lower. In Figures 17 and 18, the tangential and axial rms velocities of the preceding measurements are shown. As opposed to the mean velocities, the rms values are clearly affected by the fibers, except at 41 rps, where the difference is rather small. At lower rotational speeds, the turbulence becomes increasingly suppressed. Comparing Figures 17 and 18 reveals an increasing degree of anisotropy for larger rotational speeds. Further, the anisotropy is larger for the fiber suspension than for pure liquid. All of the measurements were made on the same suspension in the following order: 28, 25, 20, 17, 14 and 41 rps. The order was chosen to avoid mistaking fiber degradation for a decrease in the influence of the fibers. The degradation of the fibers in this run is discussed in a later section.

Turbulence spectra

Spectra were calculated from a time series of measurements at a single position. According to the Taylor hypothe-

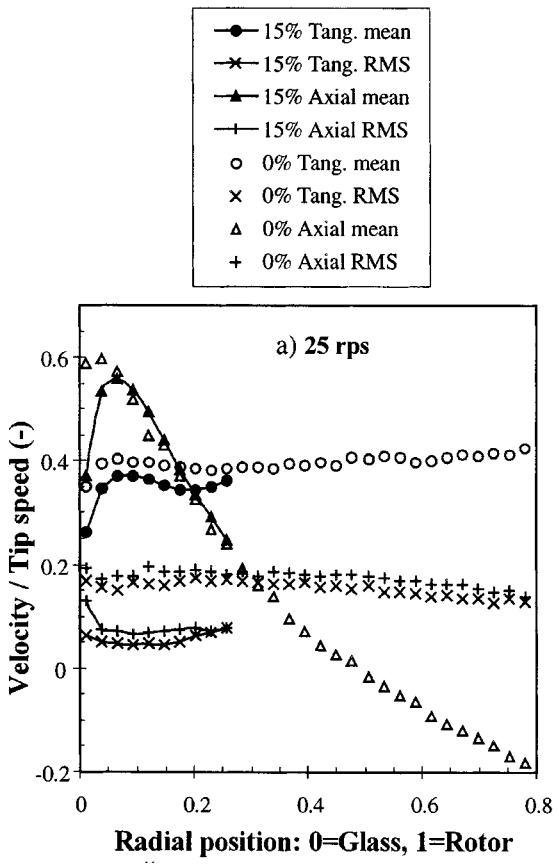

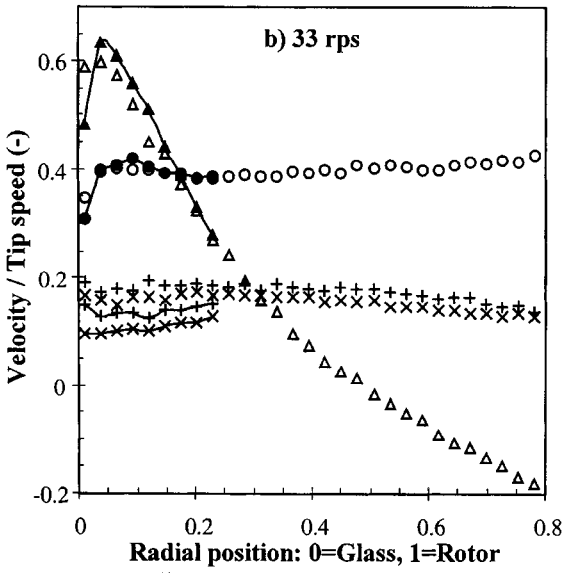

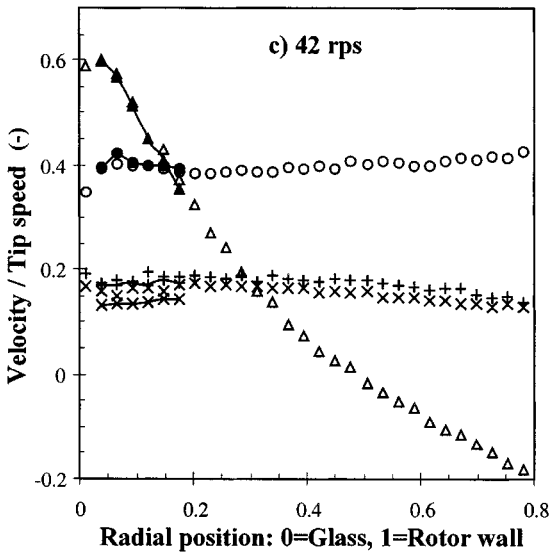

Figure 15. Radial, dimensionless, velocity profiles of single-phase flow and a 15% fiber suspension.

(a) 25 rps (just above the "fluidization" point), (b) 33 rps (just below the transition to fully turbulent flow); and (c) 42 rps (just above the transition to fully turbulent flow).

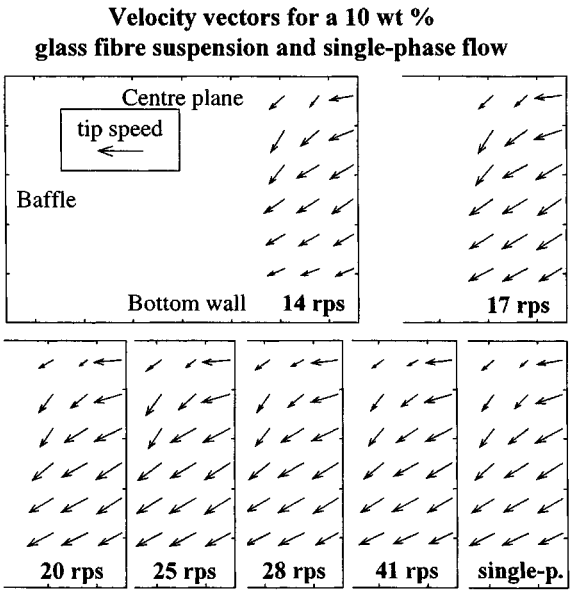

Figure 16. Vector plots of velocities in a 10 wt. % fiber suspension scaled with tip speed in a plane parallel to the observation glass at a distance of 7.7 mm from the glass.

The lowest position was 9 mm from the bottom and the rightmost position was 1 mm from the baffle. The grid spacing was 7 mm in both directions.

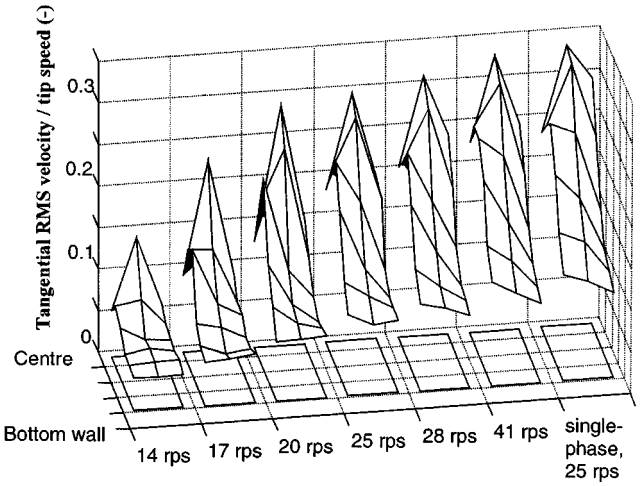

Figure 17. Rms values of the tangential velocities shown in Figure 16.

Projections of the plots are shown at the zero speed level.

sis, the time-dependent velocity signal $u(t)$ can be identified with $u(x/U)$, if $u/U \ll 1$. The area under the spectrum equals the total variance of the variable in question:

$$(u_{\text{rms}})^2 = \int_{-\infty}^{\infty} E(\kappa)\, d\kappa = [\text{Symmetrical spectrum}]$$

$$= 2 \cdot \int_{0}^{\infty} E(\kappa)\, d\kappa, \quad (7)$$

where κ is the wave number, which can be associated with eddies of size $2\pi/\ell$. Normally, when spectra are calculated from a sampled signal, the spacing of the samples is equidistant. Due to the nature of the laser Doppler method, the velocity is measured only when a particle enters the measuring volume, resulting in a random period of time between the samples. There are several remedies to this problem. The most widespread one is "sample-and-hold," which means that the velocity is kept constant until a new sample is recorded. It has, however, been shown by Høst-Madsen and Caspersen (1995) that this method produces biased results. They propose a new method called exponential decay together with a multiplicative correction factor, which they have shown to be unbiased. The software accompanying the DANTEC LDA system provided both methods for estimating turbulence spectra together with a number of windows for smoothening the spectra. The exponential decay and correction are, however, sensitive to noise and produced strange spectra in the case at hand. Instead, sample-and-hold was used. The window functions removed low-frequency characteristics, such as the peak from the rotor baffles, while the high-frequency part still contained considerable noise. Instead, the low-frequency part was left unchanged, and a mean value of surrounding points was used for higher frequencies. The number of surrounding points used was increased linearly with wave number. The power spectra of an 8% glass-fiber suspension at different rotational speeds is shown in Figure 19 together with Kolmogorov's $-5/3$ law. Strong suppression of the turbulence can be noted at low rotational speeds and wave numbers smaller than 2000: this roughly corresponds to the floc size, which was approximately 3 mm. The relatively large power at wave numbers larger than 2000 could be a result of the high shear rate expected between the flocs.

A wave number of 120 corresponds to the distance between the rotor tips; this peak is shifted toward larger wave numbers for the lowest spectra, since the mean velocity of the suspension was much lower.

Boundary-layer measurements

Measuring only one velocity component in the boundary layer allows improved refractive-index matching compared to the simultaneous matching of two components with slightly different optimal refractive indices. This allows measurements to be made at greater penetration depths. The tangential velocity component of the boundary-layer was measured by traversing the LDA probe at a step length, which decreased as the wall was approached. The reason for this was that the velocity gradient gets greater close to the wall. The velocity gradient is constant in the viscous sublayer, which enabled both the friction velocity u^* and the wall position to be determined. The procedure for doing this was to fit the y-value of the wall position together with u^*, until $u^+ = y^+$. This was an iterative procedure, since the determination of which data points should be included depended on the fit. This procedure was a prerequisite for accurate determination of the wall position, since the repeatability of the traversing system was 40 μm. For comparison, the viscous sublayer was less than 200 μm for single-phase flow at 33 rps.

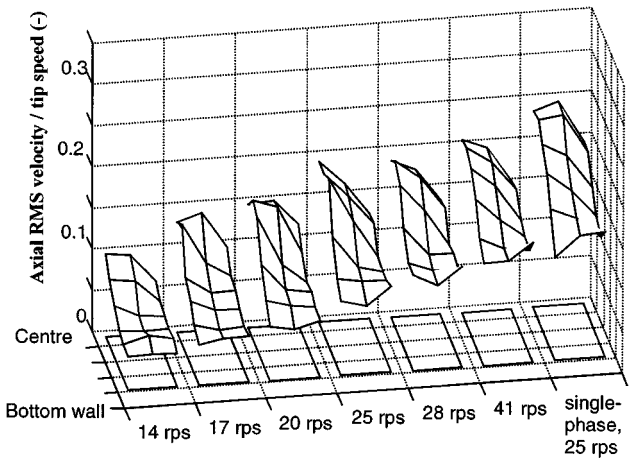

Figure 18. Rms values of the axial velocities shown in Figure 16.

Projections of the plots are shown at the zero speed level.

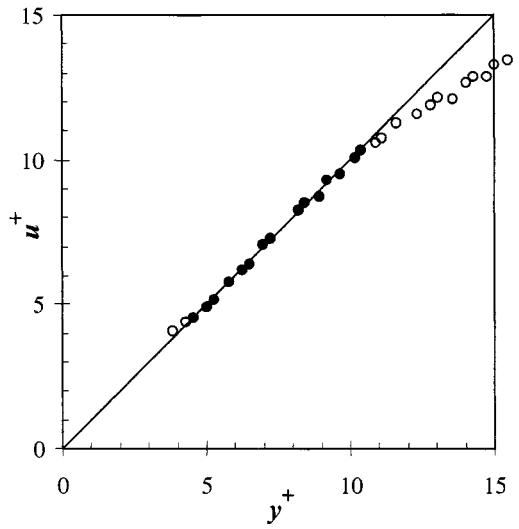

Figure 20. Resulting plot for u^+ and y^+ at 25 rps.

The measured suspension consisted of 5%, 1.5-mm fibers. The filled circles were used for determining the wall shear stress and the wall position.

The $u^+ - y^+$ plot resulting from the fitting procedure is shown in Figure 20. The filled circles were used for determining the wall shear stress and the wall position. The tangential shear stresses of single-phase flow at 17 rps is shown in Figure 21. The magnitude agrees well with the CFD (k-ϵ) values, but the trend differs somewhat.

The boundary layers of 5 wt. % glass-fiber suspensions were measured for two fiber lengths: 3 and 1.5 mm. The tangential velocities are shown in Figures 22 and 23 for single-phase flow and the two fiber suspensions at 25 rps. It can be seen that the flow profile is flatter for 3-mm fibers, which can be attributed to the increase in momentum transfer due to the fibers. The effect is present, although less pronounced, for the 1.5-mm fibers. Further, the turbulence is slightly suppressed for the 3-mm fibers, since the rotational speed is close to that of the transition to fully turbulent flow. The 1.5-mm fibers lie well above this transition. The wall shear stress from the fluid is plotted for single-phase flow and the two fiber suspensions at varying rotational speeds, as shown in Figure 24. The flatter velocity profiles of the fiber suspensions lead to a lower velocity gradient and wall shear stress, which can be seen in the figure.

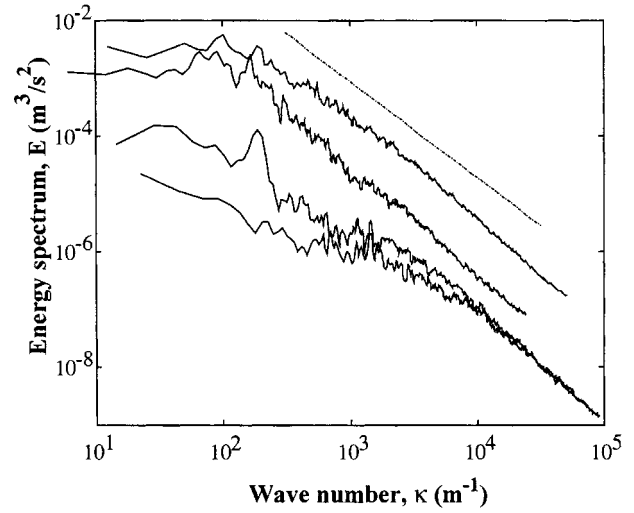

Figure 19. Power spectrum of (from above): $E \propto \kappa^{-5/3}$, single-phase flow at 33 rps and 8 wt. % glass fibers at 24, 14 and 12 rps.

Fiber degradation

The same sequence of tests was made for each concentration in order to make the different experiments comparable to each other. As the transition to turbulence was judged to be the measurement most sensitive to fiber degradation, this test was performed first. Then, the radial velocity profiles were determined for fully turbulent transition and for the suspension close to clogging. Fresh 1.5-mm and 3-mm fibers are shown in Figure 25 together with fibers degraded in the

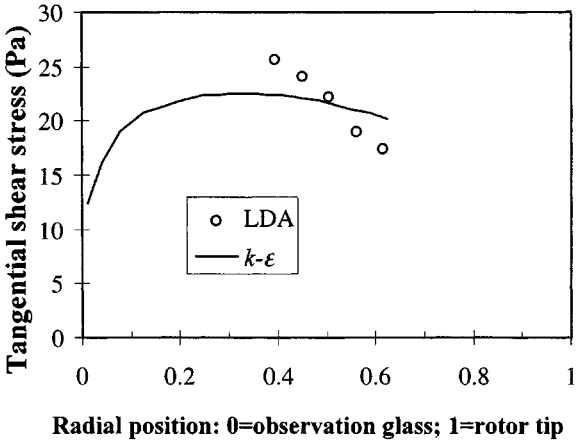

Figure 21. Measured and calculated tangential shear stresses of single-phase flow at 17 rps.

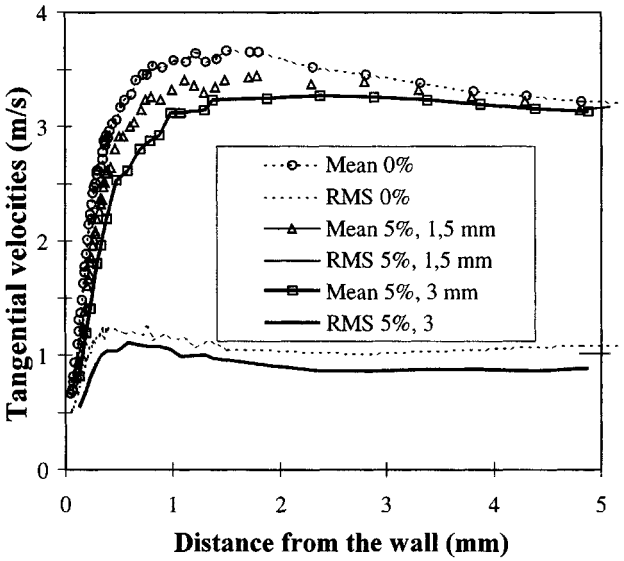

Figure 22. Tangential velocities at 25 rps, centered at a radial position of 0.5.

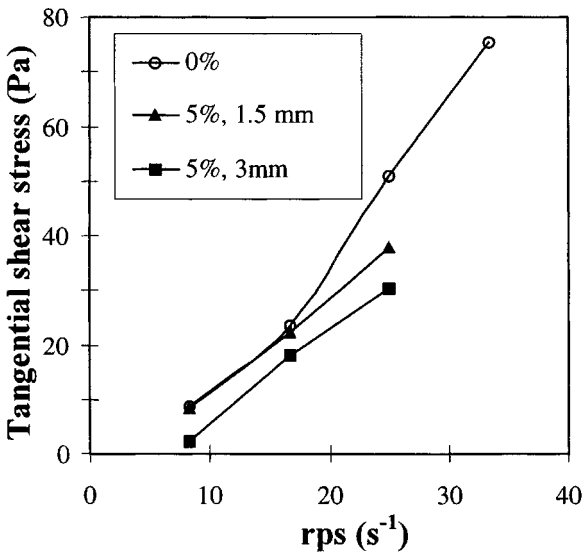

Figure 24. Tangential wall shear stress from the fluid as a function of rotational speed at a radial position of 0.5.

The lowest value is represented by 3 mm at a rotational speed, which is close to that of "fluidization."

mixer for 21 min. at 10 wt. %. The transition point determinations were made in a fraction of that time.

Discussion

Using a model system inevitably raises the question of relevance to the system of interest. In this case, the model fibers differ from pulp fibers by being straight, smooth, and having a narrow length distribution. The elastic modulus is larger for the glass fibers, but the diameter was chosen to make the stiffness comparable. The diameter of the glass fibers is therefore smaller by a factor of 3, but as the liquid viscosity is larger in the model system, viscous drag on the fibers might be of the same order of magnitude. The fiber–fluid density ratio is 2.5 for the glass-fiber suspension, while it is 1–1.5 for pulp-fiber suspensions. In a fiber suspension at high concentrations, however, the fibers are constrained by other fibers, which makes the forces from neighboring fibers important. The glass fibers are straight and smooth, whereas the pulp fibers have kinks and curls. It is therefore possible that, once the network has been disrupted in a glass-fiber suspension, a shearing surface with very low network strength is formed, while pulp fibers still can hook into each other. This could explain the large discrepancy in network strength between glass and pulp suspensions at the same concentration, found, for example, in Figure 10. In a turbulent suspension, however, eddies are continuously being formed and reshaped into smaller eddies; the shearing surfaces pictured earlier might never establish.

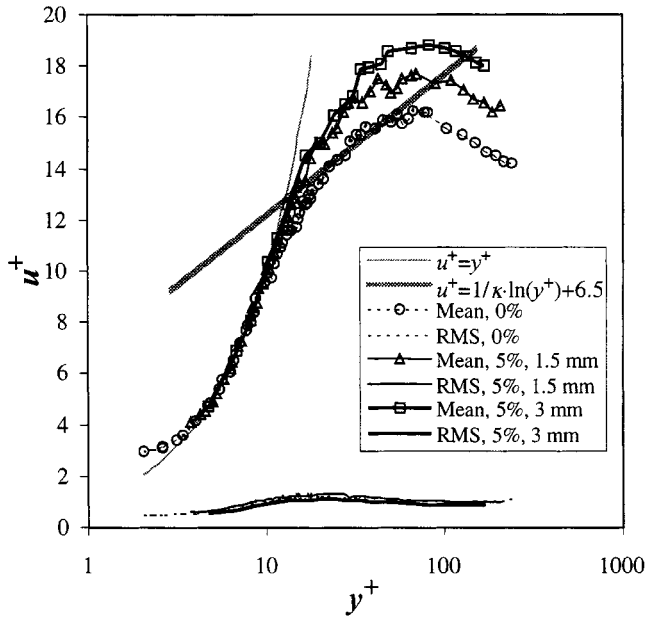

Figure 23. Tangential, dimensionless velocities at 25 rps, centered at a radial position of 0.5.

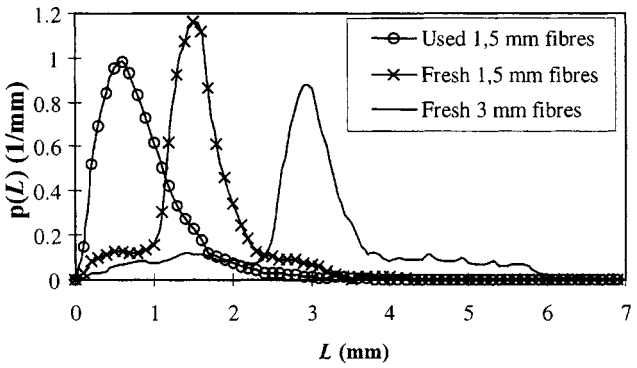

Figure 25. Length distributions of fresh 3- and 1.5-mm fibers together with fibers degraded in the mixer for 21 min at 10 wt. % and varying rps.

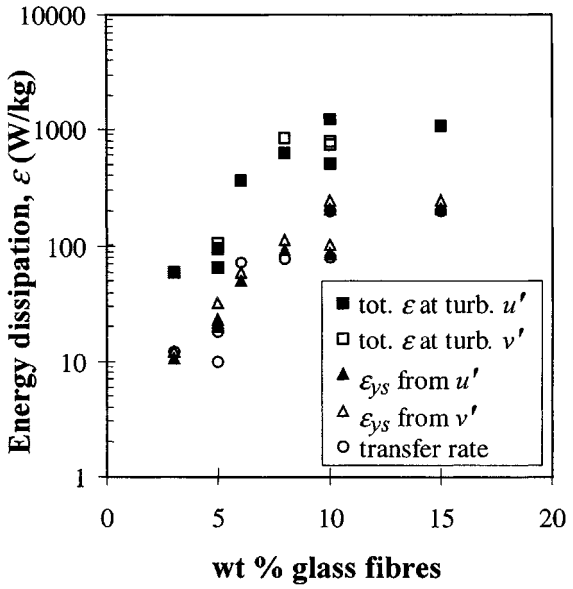

Figure 26. Total energy dissipation, ϵ, the frictional dissipation from the largest eddies, ϵ_{ys}, and the transfer rate from the largest eddies (estimated to be 30 mm).

$$\frac{\text{Inertial forces}}{\text{Yield stress}} = \frac{\rho(U_{tip})^2}{\tau_y}$$

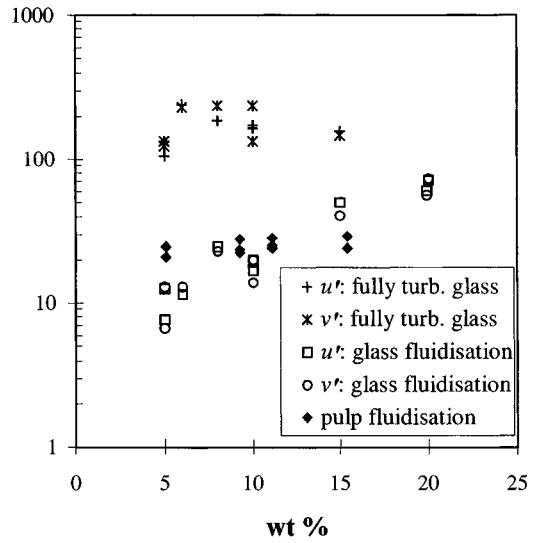

Figure 27. Dimensionless ratio of inertial forces to network strength plotted against mass concentration.

Momentum transfer in fiber suspensions

In regions of low shear rate, the yield stress has been shown by Wikström and Rasmuson (1998) to be the governing parameter for describing the flow. They measured the flow of a pulp suspension agitated by a jet nozzle with a sonar Doppler. The measurements agreed fairly well with CFD calculations made for a Bingham fluid with the yield stress of the fiber suspension. The chosen viscosity was shown to have a minor effect on the flow field. It can therefore be concluded that the dominant mechanism for momentum transfer at low shear rates arise from the elastic and frictional forces, causing fiber network strength.

Comparisons have been made between the flow of a fiber suspension at different concentrations and single-phase flow. It has been shown that a flow regime exists where the mean velocities and the fluctuating velocities are comparable to those of single-phase flow. In an intermediate region, the turbulence is severely suppressed while the flow field is close to that of fully developed turbulence.

The total energy dissipation at the transition to fully turbulent flow is plotted in Figure 26 together with the estimates for ϵ_{ys} (Eq. 4) and the energy transfer rate given by u^3/ℓ. At the fluidization point, $\epsilon_{ys} \approx u^3/\ell$, since the eddies then will lose the same amount of energy to the network as they do to the smaller eddies. The total dissipation is approximately one order of magnitude larger than ϵ_{ys} and the transfer rate. This indicates that some of the turbulent energy is created at smaller scales than the largest: presumably at the scale of the rotor vane, which is 10 mm.

Equation 5 was used to estimate the fluid velocity required for fiber sliding. The minimum force required for wet Kraft pulp fibers to slide was approximately 0.03 mN (Andersson et al., 2000). A segment length of 0.2 mm, which is a typical value (Andersson et al., 1999), and diameter of 30 μm, together with a C_D of 0.5 yields a velocity of 6 m/s. Considering that no measured rms velocities exceeded 3 m/s, very few eddies at the size of one segment length should have a velocity of 6 m/s. It therefore seems as if this mechanism plays a minor role.

The ratio of inertial forces to yield stress forces, $\rho u^2/\tau_y$, is thought to be of great importance for the turbulent structure, and should correlate to the flow transitions. The ratio is plotted in Figure 27 and is fairly constant for the pulp fluidization transitions and the transitions to fully turbulent flow, even though it increases with concentration for the glass-fiber fluidization points.

The presence of fibers increases the momentum transfer near the wall. This manifests itself by producing flatter velocity profiles, which means lower velocity gradients at the wall. It is, however, possible that the frictional-force wall fiber is large, which may lead to a larger total wall shear stress than for single-phase flow. The shear stress values were found to agree fairly well with CFD predictions for single-phase flow.

Conclusions

The LDA technique was shown to be applicable at mass concentrations up to 20 wt. %, but only with strong limitations in penetration depth, partly due to the difficulties of removing all of the air in the suspension. The values for 20% should be handled with care; fully turbulent flow was not reached at this concentration. The method worked well up to 15 wt. %.

At low rotational speeds, a portion of the suspension is stagnant, due to the network strength. As the rotation rate increases, the stagnant region decreases until it disappears

entirely and the entire suspension is flowing. This point coincides with a sudden increase in torque and was previously considered to be a transition to fully turbulent flow or fluidization. LDA measurements showed, however, that the fluctuating velocities are close to zero at this transition, while the flow field is close to that of fully turbulent flow.

The fluctuating velocities approach those of single-phase flow with increasing rotational rates until a transition to fully turbulent flow occurs. The main conclusion is that the flow of fully turbulent fiber suspensions resembles that of single-phase flow with respect to mean and rms velocities. Numerical simulations of the single-phase flow with the k-ϵ turbulence model yielded acceptable values of k, whereas the mean velocities were approximately 25% too low. The general flow pattern was, however, predicted well. The mean velocities predicted by the differential Reynolds stress model deviated slightly more from the measurements than did the k-ϵ model, while the rms values were far too low.

LDA measurements were successfully performed in the turbulent boundary-layer of fiber suspensions. In general, the linear velocity profile, $u^+ = y^+$, is obtained in the immediate proximity of the wall in the presence of fibers. The shear stress values were found to compare well with single-phase flow.

Acknowledgments

Financial support of this project has been generously provided by the Swedish Pulp and Paper Research Foundation. Owens-Corning has kindly provided the glass fibers.

Notation

C_D = drag coefficient
d = fiber diameter, m
D = vessel diameter, m
k = turbulent kinetic energy, m^2/s^2
u' = tangential rms velocity, m/s
$u^+ = u/u^*$ = dimensionless velocity
v' = axial rms velocity, m/s
y = distance from the wall, m
$y^+ = u^* \cdot y/\nu$ = dimensionless distance from the wall

Greek letters

ϵ = energy dissipation, m^2/s^3
$\kappa_{\text{Kármán}}$ = von Kármán constant = 0.4
μ = viscosity, Pa·s
ρ = density, kg/m^3
τ_y = yield stress, Pa
ν = kinematic viscosity, m^2/s

Literature Cited

Andersson, S. R., and A. Rasmuson, "Dry and Wet Friction of Single Pulp and Synthetic Fibers," *J. Pulp Paper Sci*., **23**, J5 (1997).

Andersson, S. R., T. Nordstrand, and A. Rasmuson, "The Influence of Some Fibre and Solution Properties on Pulp Fibre Friction," *J. Pulp Paper Sci*., **26**, 67 (2000).

Andersson, S. R., J. Ringnér, and A. Rasmuson, "The Network Strength of Unflocculated Fibre Suspensions," *Nordic Pulp Paper Res. J*., **14**, 61 (1999).

Bennington, C. P. J., R. J. Kerekes, and J. R. Grace, "The Yield Stress of Fibre Suspensions," *Can. J. Chem. Eng*., **68**, 748 (1990).

Bennington, C. P. J., R. J. Kerekes, and J. R. Grace, "Motion of Pulp Fibre Suspensions in Rotary Devices," *Can. J. Chem. Eng*., **69**, 251 (1991).

Bennington, C. P. J., G. Azevedo, D. A. John, S. M. Birt, and B. H. Wolgast, "The Yield Stress of Medium Consistency and High Consistency Mechanical Pulp Fibre Suspensions at High Gas Contents," *J. Pulp Paper Sci*., **21**, J111 (1995).

Bennington, C. P. J., and R. J. Kerekes, "Power Requirements for Pulp Suspension Fluidization," *TAPPI J*., **79**, 253 (1996).

Clark, M. M., "Critique of Camp and Stein's RMS Velocity Gradient," *J. Environ. Eng*., **111**, 741 (1985).

Duffy, G. G., "Flow of Medium Consistency Wood Pulp Fibre Suspensions," *Appita*, **46**, 507 (1993).

Ek, R., K. Moller, and B. Norman, "Measurement of Velocity and Concentration Variations in Dilute Fibre/Air Suspensions Using a Laser Doppler Anemometer," *TAPPI J*., **61**, 49 (1978).

Enwald, H., E. Peirano, and A.-E. Almstedt, "Eularian Two-Phase Flow Theory Applied to Fluidization," *Int. J. Multiphase Flow*, **22**, 21 (1996).

Gullichsen, J., and E. Härkönen, "Medium Consistency Technology, I. Fundamental Data," *TAPPI J*., **64**, 69 (1981).

Høst-Madsen, A., and C. Caspersen, "Spectral Estimation for Random Sampling Using Interpolation," *Signal Process*., **46**, 297 (1995).

Kerekes, R. J., and R. G. Garner, "Measurement of Turbulence in Pulp Suspensions by Laser Anemometry," *Trans. Tech. Sect. CPPA*, **8**, TR53 (1982).

Li, T.-Q., J. D. Seymour, R. L. Powell, M. J. McCarthy, K. L. McCarthy, and L. Ödberg, "Visualization of Flow Patterns of Cellulose Fiber Suspensions by NMR Imaging," *AIChE J*., **40**, 1408 (1994).

McComb, W. D., *The Physics of Fluid Turbulence*, Oxford Science Publications, Oxford (1991).

Owens-Corning Fiberglass Corporation, *Textile Fibres for Industry*, Brochure, Owens-Corning World Headquarters, Toledo, OH (1994).

Schlichting, H., *Boundary-Layer Theory*, McGraw-Hill, New York (1966).

Steen, M., "The Application of Refractive Index Matching for Two-Phase Flow Measurements in Turbulent Fibre Suspensions by Laser Doppler Anemometry," *Nordic Pulp. Paper Res. J*., **4**, 236 (1989a).

Steen, M., "On Turbulence Structure in Vertical Pipe Flow of Fibre Suspensions," *Nordic Pulp Paper Res. J*., **4**, 244 (1989b).

Tennekes, H., and J. L. Lumley, *A First Course in Turbulence*, 14th print., MIT Press, Cambridge, MA (1992).

Wahren, D., "Fiber Network Structures in Papermaking Operations," *Proc. I.P.C. Conf. on Paper Science and Technology*, Appleton (1980).

Wikström, T., and A. Rasmuson, "The Agitation of Pulp Suspensions with a Jet Nozzle Agitator," *Nordic Pulp Paper Res. J*., **13**, 88 (1998).

Manuscript received Feb. 17, 1999, and revision received Jan. 4, 2000.